Design of an Integrated Bell-State Analyzer on a Thin-Film Lithium Niobate Platform

Uday Saha, *Student Member, IEEE*, and Edo Waks

***Abstract*—Trapped ions are excellent candidates for quantum computing and quantum networks because of their long coherence times, ability to generate entangled photons as well as high fidelity single- and two-qubit gates. To scale up trapped ion quantum computing, we need a Bell-state analyzer on a reconfigurable platform that can herald high fidelity entanglement between ions. In this work, we design a photonic Bell-state analyzer on a reconfigurable thin-film lithium niobate platform for polarization-encoded qubits. We optimize the device to achieve high fidelity entanglement between two trapped ions and find >99% fidelity. Apart from that, the directional coupler used in our design can achieve any polarization-independent power splitting ratio which can have a rich variety of applications in the integrated photonic technology. The proposed device can scale up trapped ion quantum computing as well as other optically active spin qubits, such as color centers in diamond, quantum dots, and rare-earth ions.**

***Index Terms*—Bell-state analyzer, thin-film lithium niobate, scalable quantum computing, trapped ions, entanglement, polarization qubits, polarization-independent directional coupler.**

I. Introduction

TRAPPED ions are one of the most advanced platforms for quantum computing and quantum networks. They exhibit long coherence times [1]–[3], naturally emit photons entangled with their internal qubit memories [4]–[6], and support high-fidelity single- and two-qubit gates [7], [8]. Apart from that, they can be trapped in a compact surface electrode ion-trap with integrated waveguides and grating couplers for ionization, cooling, coherent operation and quantum state preparation, and detection [9]. But quantum computers and networks based on trapped ions also require photonic devices in order to interconnect different nodes of the network [10], [11]. The key optical component in these devices is the photonic Bell-state analyzer [12], which heralds the successful entanglement between distant qubits. Such entanglement provides a photonic interconnect between trapped ions, which can be used to scale up trapped ion quantum computers [2], [13] as well as enable long-distance quantum networks [10], [14]–[16]. But to realize these interconnects in a scalable way requires compact reconfigurable chip-integrated devices that can perform Bell-state analysis between trapped ions at different nodes [10], [14].

Thin-film lithium niobate is a promising material platform to implement photonic Bell analyzers on a compact chip. Lithium niobate has a broad transparency window over the visible spectrum [17], making it compatible with many ion species. It also possesses a high electro-optic coefficient, which enables reconfigurable photonic devices with ultra-fast switching speed [18], [19]. Moreover, it has excellent thermo-optic and piezoelectric properties for nanophotonic applications [20]. Recent progress in fabrication has enabled ultra-low loss thin-film lithium niobate waveguides in both the visible [17] and telecom range [21]. Apart from that, thin-film lithium niobate can be used for quantum frequency conversion which is beneficial for implementing quantum networks [16], [22]–[24].

But applying thin-film lithium niobate devices to photons generated by trapped ions is challenging because trapped ions naturally emit polarization-encoded photonic qubits [25], [26]. Thin-film lithium niobate waveguides possess small sidewall angles [27] and require partial etching to achieve low waveguide loss [17], [21]. These properties create a large polarization anisotropy, which makes it difficult to engineer a photonic Bell-state analyzer for polarization qubits. In particular, the Bell-state analyzer typically employs a non-polarizing beam splitter, which is hard to engineer with a highly anisotropic device structure. Previously, slot waveguides have been developed in the silicon technology [28]–[30] to achieve polarization-insensitive on-chip components that could be used for Bell-state analysis. Due to low index-contrast and reactive ion etching technique [17], it is hard to engineer slot waveguide structure in thin-film lithium niobate to achieve polarization-insensitive operation. Recently, polarization-insensitive modulators and switches have been achieved in a bulk lithium niobate [31] and hybrid silicon and lithium niobate platform [32] using polarization diversity where two orthogonal polarizations have been modulated separately. Very recently, Zhang *et al.* [33] designed a polarization-insensitive directional coupler with fully etched ridge waveguide structure which can suffer high waveguide loss [17], [21], [34]. Apart from that, two orthogonal polarizations can experience different sidewall surface roughness in a fully etched ridge waveguide structure

Manuscript received September 22, 2021; revised November 30, 2021; accepted December 15, 2021. Date of publication December 17, 2021; date of current version January 4, 2022. This work was supported in part by the National Science Foundation under Grants EFMA1741651 and OIA2040695, and in part by the Air Force Office of Scientific Research under Grants FA95501610421 and FA95501810161. *(Corresponding author: Edo Waks.)*

Uday Saha is with the Department of Electrical and Computer Engineering, University of Maryland, College Park, MD 20742 USA, and also with the Institute for Research in Electronics and Applied Physics, University of Maryland, College Park, MD 20742 USA (e-mail: uday@umd.edu).

Edo Waks is with the Department of Electrical and Computer Engineering, University of Maryland, College Park, MD 20742 USA, with the Institute for Research in Electronics and Applied Physics, University of Maryland, College Park, MD 20742 USA, and also with the Joint Quantum Institute, University of Maryland, College Park, MD 20742 USA (e-mail: edowaks@umd.edu).

Digital Object Identifier 10.1109/JPHOT.2021.3136502

which can induce polarization-dependent losses making the structure polarization-sensitive. Polarization-insensitive operation with partial etching and small sidewall angles required for low waveguide loss in thin-film lithium niobate, has not been reported yet for polarization qubits. Although in principle it is possible to convert polarization qubits to time-bin qubits, the relatively long excited-state lifetimes of trapped ions [35] would necessitate impractically large on-chip delay lines. Realizing a photonic Bell-state analyzer with polarization-encoded qubits in thin-film lithium niobate would therefore be an important step towards applying this powerful platform to trapped ion quantum interconnects.

In this work, we propose and analyze a design for a photonic Bell-state analyzer for polarization-encoded qubits in thin-film lithium niobate with a partially etched rib waveguide structure and small sidewall angles. To overcome the polarization anisotropy, we optimize the dimensions of the device to achieve the desired unitary operation of the transverse electric (TE) and transverse magnetic (TM) polarization components simultaneously. We design the Bell-state analyzer to operate at the main transition wavelength (493.55 nm) of trapped barium ions ($^{133}Ba^+$ and $^{138}Ba^+$), which are a leading candidate for optically active qubits for trapped ion quantum computing [2], [36]. We further optimize the input coupler to achieve nearly identical light coupling efficiencies for the TE and TM modes (66.16% and 65.52%, respectively). Our numerical analysis shows the optimized device can mediate entanglement between distant ions with fidelities exceeding 99%. Moreover, we achieve arbitrary polarization-independent power splitting ratio by adjusting the coupling length of the device. The proposed Bell-state analyzer provides a promising approach to interconnect trapped ions, which would enable the scaling of trapped ion quantum computers [2], [13] as well as other optically active spin qubits such as color centers in diamond [37], quantum dots [38], and rare-earth ions [39].

II. Device Structure

Fig. 1 illustrates the operating principle of the photonic Bell-state analyzer and how it mediates entanglement between trapped ions. The Bell-state analyzer is composed of a non-polarizing 50/50 beam splitter and photon detectors. Each ion emits a spin-photon with an entangled quantum state given by $|\psi\rangle = |\uparrow\rangle|V\rangle + |\downarrow\rangle|H\rangle$ where $|\uparrow\rangle$ and $|\downarrow\rangle$ represent the spin up and spin down states of the ions, and $|H\rangle$ and $|V\rangle$ denote two orthogonal polarization states of the emitted single photons. The photon from each ion is injected into the respective input port of the beam splitter. A coincidence detection event between the two detectors heralds a projective measurement of the two-photon state onto the Bell-state $|\psi^-\rangle_p = \frac{1}{\sqrt{2}}(|HV\rangle - |VH\rangle)$ [5]. If no coincidence is detected, the measurement produces an inconclusive result. Although this measurement is probabilistic, it is sufficient to herald entanglement between ions in order to scale up trapped ion quantum computers [2], [13] or establish a quantum network [14]. Improved configurations can yield higher efficiencies [40], but in this work we will consider this simple Bell analyzer device.

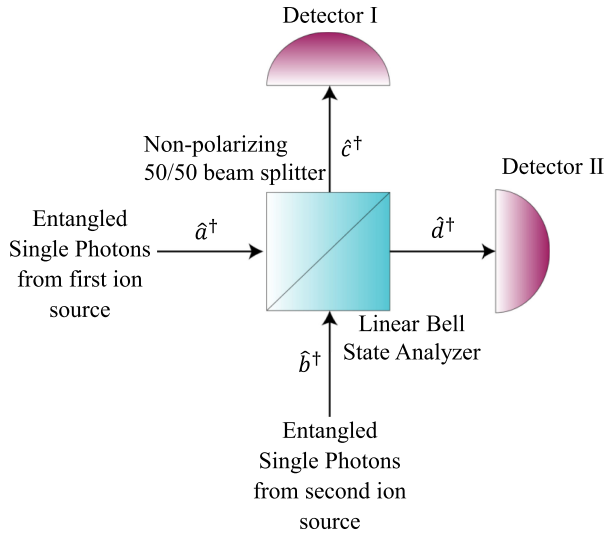

Fig. 1. Entanglement experiment of two ions through quantum interference on a non-polarizing 50/50 beam splitter. Here, $\hat{a}^\dagger$ and $\hat{b}^\dagger$ represent the input bosonic operators and $\hat{c}^\dagger$ and $\hat{d}^\dagger$ are the output bosonic operators.

Although conceptually simple, chip-integration of this device is challenging due to the requirement that the beam splitter must be non-polarizing. To satisfy this requirement, we consider the directional coupler structure shown in Fig. 2(a), which acts as an on-chip beam splitter. The directional coupler is composed of two waveguides that are brought together at a coupling region of length L_c, where they can interact through their evanescent fields. Each waveguide supports a TE and TM mode, which define the polarization qubit basis of a propagating photon. The two input modes enter through ports 1 and 2, and the two output modes leave through ports 3 and 4, as illustrated in Fig. 2(a). Photodetectors at the output ports herald entanglement generation. To connect these ports to the coupling region, we use S bends that taper the initial distance (y) of 2 μm between the waveguides over a distance of L_s. To generate a S bend, we use a Bezier curve with 4 points located at $(-L_s/2, -y/2)$, $(0,-y/2)$, $(0,y/2)$, $(L_s/2, y/2)$. Fig. 2(b) shows the cross-sectional view of the device structure in the coupling region. The layer structure is composed of 300 nm thick X-cut lithium niobate on 2 μm thick silicon dioxide (SiO_2). Each waveguide is formed from a partially etched rib waveguide structure with 75° side angles [27] and partial etch depth and width of h_e and w, respectively. We define the slab thickness as $h_{slab} = (300 - h_e)$ nm. The waveguides are separated by a gap distance of g. They are also encapsulated in a 2 μm thick SiO_2 cladding layer.

III. Results and Discussion

The goal is to design a beam splitter that exhibits 50/50 power splitting ratios for both TE and TM modes. To gain a better understanding of how to achieve this condition, we apply coupled mode theory to analyze the coupling region of the device [41]. The coupled waveguides form two new modes, a symmetric and anti-symmetric mode (Fig. 7 in the Appendix A). The power splitting between the waveguides depends sinusoidally on the

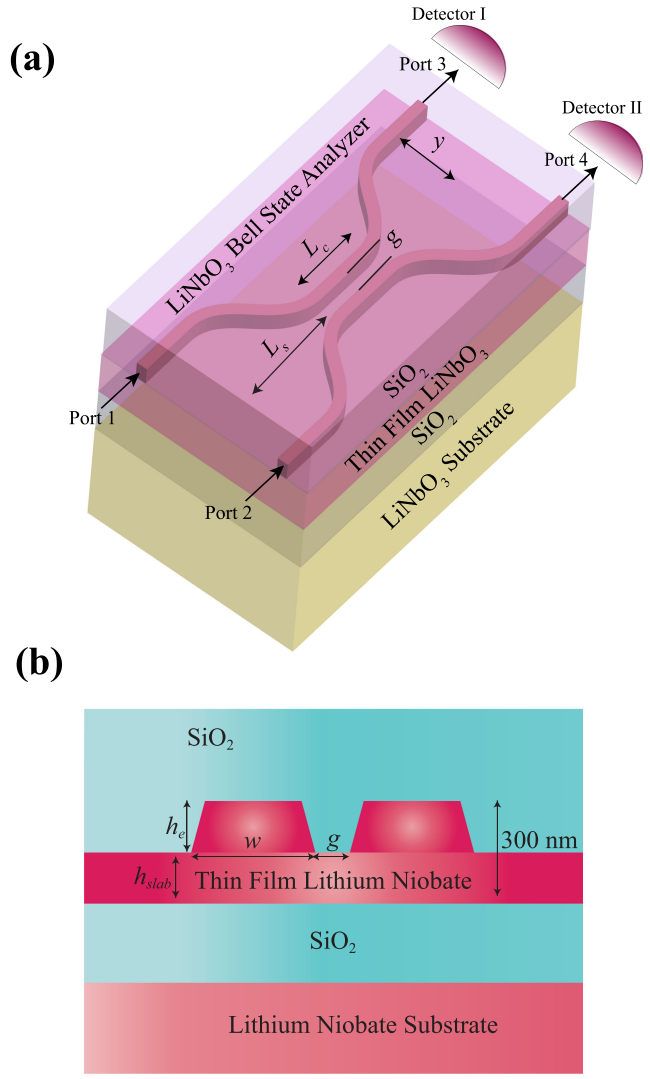

Fig. 2. (a) 3D schematic of the proposed non-polarizing on-chip beam splitter fabricated on a thin-film lithium niobate platform. (b) Cross-sectional view of the non-polarizing beam splitter in the coupling region.

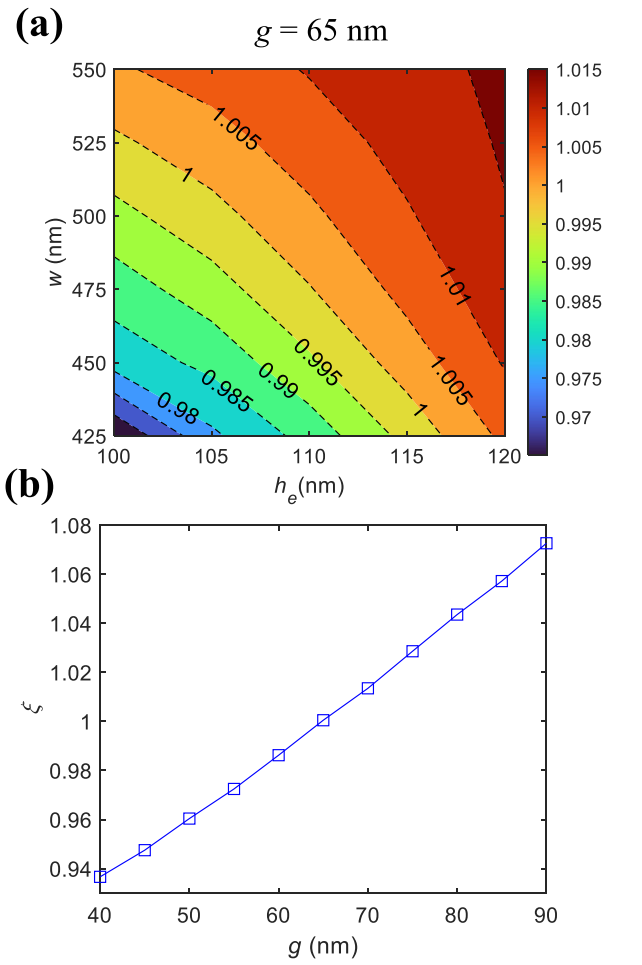

Fig. 3. The change in ξ as a function of (a) the width (w) and etch depth (h_e) of the non-polarizing beam splitter at $g = 65\ nm$ and (b) as a function of the gap distance (g) at $w = 475\ nm$ and $h_e = 110\ nm$. Here, markers are the simulated values of ξ and solid blue line represents the fitted line through those data points showing the dependence of ξ with respect to g.

difference of the effective refractive indices of these modes (Δn), which we define as the coupling factor. If light is initially injected into port 1 with power P_I, then the power in ports 3 and 4 are given by $P_3 = P_I \cos^2(\frac{\pi \Delta n}{\lambda_0} L_c)$ and $P_4 = P_I \sin^2(\frac{\pi \Delta n}{\lambda_0} L_c)$, where λ_0 is the operating wavelength.

Due to the large anisotropy in the shape of the waveguides, the TE and TM modes will in general have different Δn, which will lead to different power splitting ratios for the two polarizations. To achieve a non-polarizing beam splitter, we need to first minimize this disparity. We denote Δn_{TE} and Δn_{TM} as the coupling factor for the TE and TM modes, respectively. We define the ratio $\xi = \frac{\Delta n_{TE}}{\Delta n_{TM}}$ as the figure of merit for our device, with the optimal device achieving $\xi = 1$.

We calculate ξ using a finite difference eigenmode solver (Lumerical Mode solutions). To avoid material anisotropy of lithium niobate, we consider X-cut lithium niobate where light is propagating along Z- axis so that TE and TM polarized light experience the ordinary refractive index of 2.34 [42], [43]. In this respect, the difference of ordinary and extraordinary refractive indices is $\sim$0.093 [42], [43]. In our calculations, we set the refractive index of SiO_2 to be 1.462 [44].

To achieve $\xi = 1$, we vary the width and etch depth of the non-polarizing beam splitter with a gap distance of $g = 65\ nm$ (Fig. 3(a)). The contour line of $\xi = 1$ passes through multiple combinations of the width and etch depth. From these combinations, we select a width of $475\ nm$ and etch depth of $110\ nm$ where $\xi = 1$. Then, we observe the effect of the gap on ξ at that width and etch depth (Fig. 3(b)). We find that ξ increases monotonically with the gap of the coupling region. We achieve $\xi = 1$ at our previous simulated gap of $65\ nm$. There are multiple combinations of the width, etch depth, and gap that can lead to $\xi = 1$ and polarization insensitivity for the coupling region of the non-polarizing beam splitter. We select a combination of $w = 475\ nm$, $h_e = 110\ nm$, and $g = 65\ nm$ for our following analysis where $\xi = 1$.

In order to design the full device, we must also consider the S bend regions (Fig. 2(a)), which can significantly contribute to the power splitting ratio. The bending regions create additional complications by introducing greater anisotropy as well as polarization-dependent loss. Using the previously optimized

width and etch depth, we optimize the bending length (L_s) to achieve minimal bending losses and a small device footprint that can route quantum information efficiently (Fig. 8 in Appendix B). We choose L_s to be 30 microns, as this value results in high transmission for both the TE and TM modes (0.993 and 0.994, respectively).

Using the previously optimized width (w), etch depth (h_e), gap (g), and bending length (L_s), we then simulate the complete device with the S-bends. To perform the simulations, we use Eigen Mode Expansion (EME) solver provided by Lumerical (we discuss the details of simulation methodology in Appendix C). To analyze the polarization-insensitive operation of the device, we investigate how the normalized power values at ports 3 and 4 change with the coupling length (L_c) for the TE and TM modes (Fig. 4(a)). In this case, the normalized power at both ports do not match for the TE and TM modes, resulting in a polarization-dependent power splitting ratio for the non-polarizing beam splitter. This problem arises because the S-bend region contributes significantly to the power coupling between the waveguides. As TE and TM polarized light have different effective refractive indices, this coupling is highly sensitive to polarization, leading to polarization-dependent power splitting for the overall device. Given the effect of the S-bend, we need to reoptimize the parameters to achieve a polarization-independent power splitting ratio for the whole device.

To achieve polarization insensitivity for the full device including the S-bends, we vary the gap, which significantly controls the power splitting ratio of the non-polarizing beam splitter, while keeping the other parameters fixed at their previously optimized values ($w = 475\ nm, h_e = 110\ nm, L_s = 30\ \mu m$). We define a polarization-dependence parameter, ζ which is the difference in the normalized powers of the TE and TM modes of port 3 at specific coupling length. Here, $\zeta = P_3^{TE} - P_3^{TM}$, where P_3^{TE} and P_3^{TM} represent the normalized power of port 3 for TE and TM modes, respectively. To achieve any arbitrary polarization insensitive power splitting ratio, we calculate the root mean square value of ζ for coupling lengths of 1 to 25 μm, which contain all the possible power splitting ratios, and define the parameter as δ. Here, δ contains the polarization dependent characteristics of non-polarizing beam splitter over coupling length of 1 to 25 μm and we express it as $\delta = \sqrt{\frac{\zeta_1^2+\zeta_2^2+\cdots\ldots+\zeta_n^2}{n}}$, where $\zeta_1, \zeta_2, \ldots\ldots\ldots\zeta_n$ represent the value of ζ at different coupling lengths and n is total number of coupling lengths over 1 to 25 μm. We then minimize δ by varying the gap, which occurs at $g = 40\ nm$ (Fig. 4(b)). Here, finite δ represents that, we can not achieve exact polarization-independent device but minimizing δ can lead us close to any polarization-independent power splitting ratio. Fig. 4(c) shows the normalized power values at ports 3 and 4 for the TE and TM modes with respect to the coupling length (L_c) at $g = 40\ nm$, which virtually overlap. As a result, we can approximately achieve any polarization insensitive power splitting ratio by varying the coupling length from 6.4 μm to 21.5 μm. These results show that in addition to achieving a 50/50 power splitting ratio, we can attain any desired ratio by varying the coupling length. This ability is key to realizing different types of photonic quantum gates for polarization-based qubits [45],

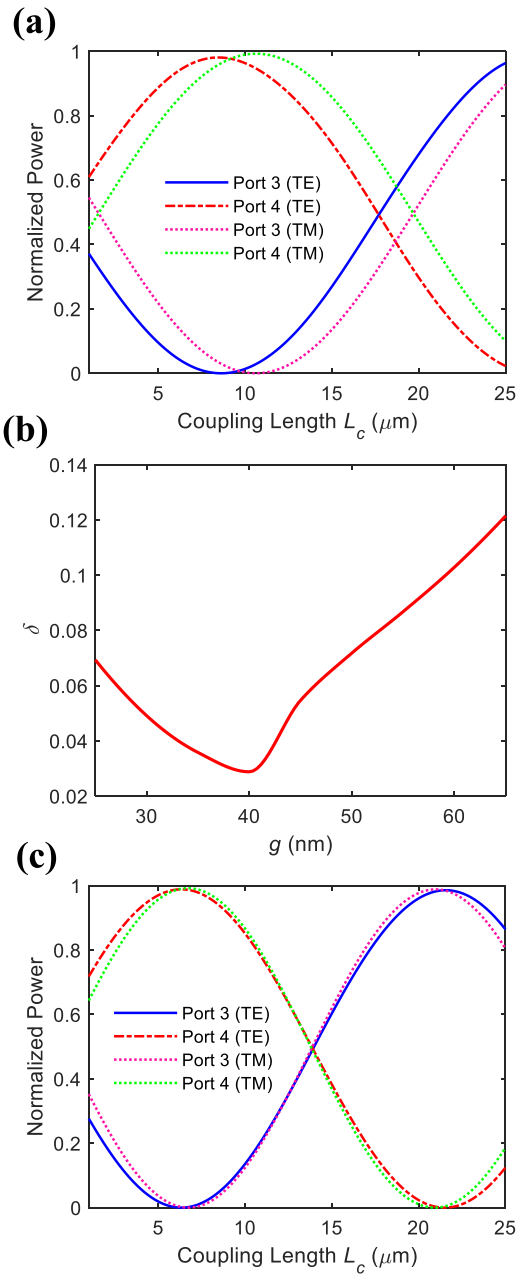

Fig. 4. (a) The change in the normalized power at ports 3 and 4 with respect to the coupling length (L_c) for TE and TM polarizations at $g = 65\ nm$. (b) The variation of δ as a function of g. Here, δ contains the polarization dependent characteristics of non-polarizing beam splitter over coupling length of 1 to 25 μm. We express it as $\delta = \sqrt{\frac{\zeta_1^2+\zeta_2^2+\cdots\ldots+\zeta_n^2}{n}}$, where $\zeta_1, \zeta_2, \ldots\ldots\ldots\zeta_n$ represent the value of ζ at different coupling lengths and n is total number of coupling lengths over 1 to 25 μm.(c) The change in the normalized power at ports 3 and 4 as a function of the coupling length (L_c) for TE and TM polarizations at $g = 40\ nm$.

[46]. Apart from that, $g = 40\ nm$ corresponds to top gap of $\sim$100 nm between the waveguides which can be realized with existing fabrication technology [17], [39], [47].

To predict our device performance for entangling two remote ions, we calculate the error in entanglement. On a beam splitter,

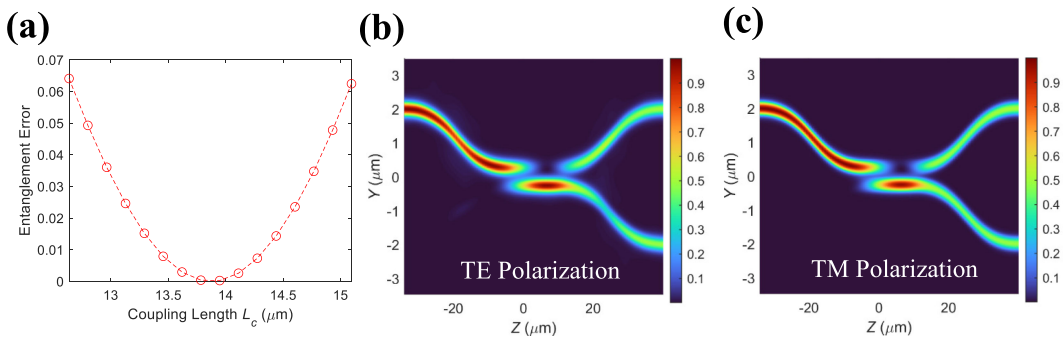

Fig. 5. (a) Variation of the error of entangling two ions as a function of L_c (from 12.5 μm to 15 μm). (b) and (c) represent the electric field propagation through the non-polarizing beam splitter at $L_c = 13.95$ μm for TE and TM polarization, respectively.

the input-output relationship can be written in the following way:

$$\begin{bmatrix} \hat{a}^{\dagger}_{h(v)} \\ \hat{b}^{\dagger}_{h(v)} \end{bmatrix} = \begin{bmatrix} t_{h(v)} & r_{h(v)} \\ r_{h(v)} & -t_{h(v)} \end{bmatrix} \begin{bmatrix} \hat{c}^{\dagger}_{h(v)} \\ \hat{d}^{\dagger}_{h(v)} \end{bmatrix} \quad (1)$$

in which $\hat{a}^{\dagger}_{h(v)}$ and $\hat{b}^{\dagger}_{h(v)}$ represent the input bosonic operators of ports 1 and 2 for horizontal (vertical) polarization and $\hat{c}^{\dagger}_{h(v)}$ and $\hat{d}^{\dagger}_{h(v)}$ are the output bosonic operators of ports 3 and 4 for horizontal (vertical) polarization. The parameters $t_{h(v)}$ and $r_{h(v)}$ are the transmission and reflection coefficients of the photonic beam splitter for horizontal (vertical) polarization, respectively. Upon simultaneous detection of photons in the detectors, we can write the detected state as

$$|\psi\rangle_{detected} = \frac{1}{r_h^2 r_v^2 + t_h^2 t_v^2}(r_h r_v |\downarrow\rangle_a|\uparrow\rangle_b - t_h t_v |\uparrow\rangle_a|\downarrow\rangle_b) \quad (2)$$

The fidelity of detecting the entangled ion state $|\psi^-\rangle_I = \frac{1}{\sqrt{2}}(|\downarrow\rangle_a|\uparrow\rangle_b - |\uparrow\rangle_a|\downarrow\rangle_b)$ will be

$$F = \|\langle\psi_I^-|\psi_{detected}\rangle\|^2 = \frac{1}{2}\frac{(r_h r_v + t_h t_v)^2}{r_h^2 r_v^2 + t_h^2 t_v^2} \quad (3)$$

Then, we define the entanglement error as

$$E = 1 - F \quad (4)$$

Fig. 5(a) depicts the error of the entanglement of the two ions as a function of the non-polarizing beam splitter's coupling length (L_c). To obtain high fidelity entanglement between two remote ions, we simulate a sweep of the coupling length from 12.5 μm to 15 μm, where a 50/50 power splitting ratio occurs, as shown in Fig. 4(c). We achieve a minimum error of 2.48×10^{-4} at $L_c = 13.95$ μm. This corresponds to a power splitting for ports 3 and 4 of 49.7/48.9 (Fig. 5(b)) and 50.7/48.3 (Fig. 5(c)) for the TE and TM modes, respectively. These findings demonstrate we can achieve a compact integrated Bell-state analyzer on a thin-film lithium niobate platform to generate high fidelity entanglement between remote qubit systems. We discuss the effect of change in the width, etch depth, slab thickness, operating wavelength, and surface roughness on the device performance in Appendix D. Fabrication imperfections can create variations in the width, etch depth, and slab thickness. In this regard, we can achieve >98% fidelity over 10 nm variation of width and etch depth. In the case of slab thickness, we can attain >96.3% fidelity over 30 nm variation. Our designed device is also broadband over 20 nm wavelength range where we can achieve >97% fidelity.

Although we design this polarization-insensitive photonic Bell-state analyzer for remote ion entanglement, coupling light into the chip independent of polarization is crucial to maintain high fidelity entanglement between ions. If the TE and TM modes couple with different efficiencies, that will destroy the polarization insensitivity of the device and reduce the fidelity of entanglement. Therefore, we analyze and optimize the coupling efficiencies for the TE and TM modes.

To couple light into the chip, we consider a specific coupling scheme based on a lensed fiber. This approach can maintain the polarization insensitivity and yield high coupling efficiencies [48]. In this scheme, a lensed fiber is edge-coupled to the chip and the fiber numerical aperture (NA) is matched to waveguide's NA. We determine the coupling efficiencies by calculating the mode overlap integral between the lensed fiber mode and waveguide mode (Fig. 6(a) and (b) represent the TE and TM modes, respectively)

Fig. 6(c) represents the light coupling efficiency for the TE and TM modes with respect to the NA of the lensed fiber. At lower NA, the gaussian beam of the lensed fiber is larger than the waveguide mode. Due to the mode mismatch, we achieve lower coupling efficiencies at lower NAs. By increasing the NA, we can decrease the mode size of the lensed fiber and make it closer to the waveguide mode to achieve higher coupling efficiencies. However, we vary up to 0.6 NA which is commercially available. At this NA value, we obtain 66.16% and 65.52% coupling efficiencies for TE and TM polarizations, respectively. Taking these coupling efficiencies into account, we further calculated the error in entanglement and found an error of 2.54×10^{-4} in entangling two remote ions. We also can achieve polarization-independent coupling of >50% with an alignment error between chip and lensed fiber (Appendix E). Through our design, we can incorporate light in a polarization-independent manner, which enables an efficient interface for transferring quantum information from polarization qubits. High efficiency light coupling is crucial for achieving high entanglement rate

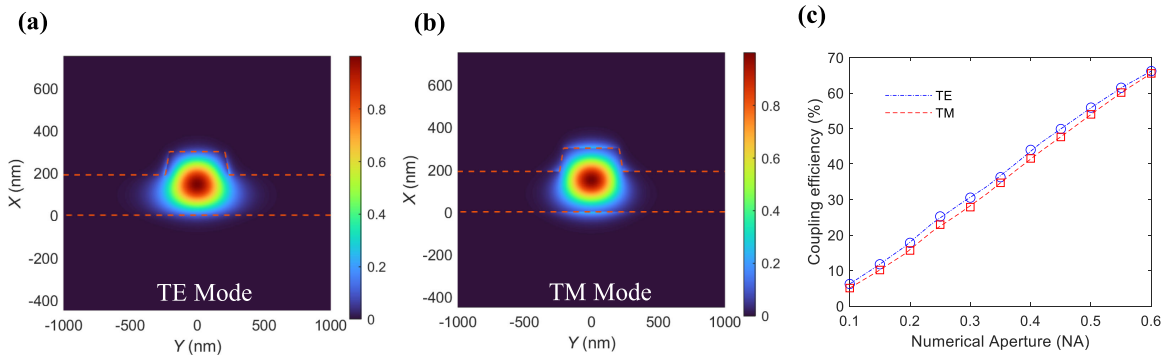

Fig. 6. (a) and (b) represent the electric field intensity of the waveguide for TE and TM polarization, respectively. (c) The change in the light coupling efficiency from fiber to chip with respect to the numerical aperture (NA) of the lensed fiber.

between ions [26]. Achieving >60% light coupling efficiency is a practically good result. Although it would lead to a <40% reduction in entanglement rate, the entanglement rate of trapped ions is far longer than the decoherence rate to tolerate this loss. To obtain higher light coupling efficiencies, other methods like tapered waveguide structure [49],grating coupler [50], and evanescent field coupling between the waveguide and conical tapered optical fibers [51], etc., can be used. These approaches might achieve even higher efficiency than what we achieve in this work but will require careful design and may be significantly more complex to fabricate and use.

IV. Conclusion

In summary, we design an integrated photonic Bell-state analyzer on a thin-film lithium niobate platform that exhibits greater than 99% fidelity for the entanglement of two remote trapped ion qubit systems. To overcome polarization-mode anisotropy, we optimize the etch depth, width, gap, bending length, and coupling length of the non-polarizing beam splitter and achieve polarization independent 50/50 power splitting and minimum error in entangling two remote ions. We also analyze and optimize the numerical aperture of a lensed fiber to achieve a polarization-insensitive light coupling interface and achieve identical coupling efficiencies for TE and TM polarizations (66.16% and 65.52%, respectively). Apart from entangling two remote trapped ions, we can achieve any polarization-independent power splitting ratios in the directional coupler by adjusting the coupling length, which can be used to realize different quantum gates and integrated photonic devices. Moreover, the design of the photonic Bell-state analyzer can be modified to create optical interconnects between optically active spin qubit systems, such as color centers in diamond, quantum dots, and rare earth ions, etc. By using electro-optic modulation, our proposed device can be engineered to act as a reconfigurable polarization-maintaining switch fabric, which may be useful for other quantum applications. Therefore, this integrated photonic Bell-state analyzer design could enable a new generation of compact and reconfigurable integrated photonic devices that can serve as efficient quantum interconnects for quantum computers and sensors.

Disclosure: The authors declare no competing financial interest.

Appendix A
Symmetric and Anti-Symmetric Modes in the Coupling Region of the Non-Polarizing Beam Splitter

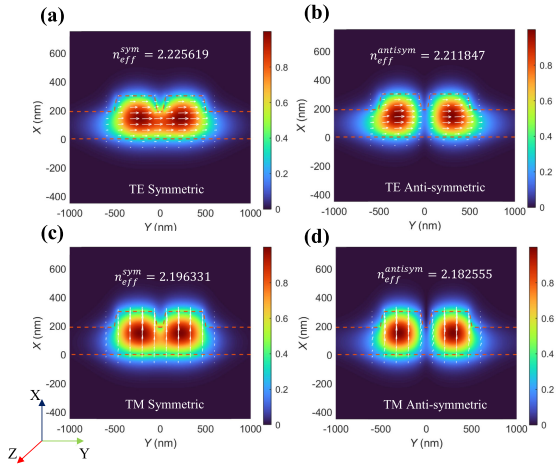

Fig. 7. Electric field distribution of the symmetric and anti-symmetric modes for the TE ((a) and (b)) and TM ((c) and (d)) polarizations, respectively, at $w = 475\ nm$, $h_e = 110\ nm$, and $g = 65\ nm$.

Appendix B
Optimizing the S Bend for Compact, Polarization-Insensitive Operation

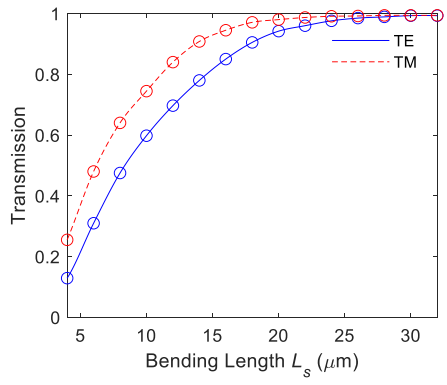

Fig. 8. Dependence of the transmission through the S bend as a function of the bending length (L_s) for the TE and TM modes.

TABLE I
COMPARISON BETWEEN EIGEN MODE EXPANSION (EME) AND FINITE DIFFERENCE TIME DOMAIN (FDTD) METHODOLOGY OF OUR FINAL SIMULATION RESULTS

Simulation Method	Transmission for Transverse Electric (TE) Polarized light (%)		Transmission for Transverse Magnetic (TM) Polarized light (%)		Fidelity of Entangling Two Trapped Ions(%)
	Port 3	Port 4	Port 3	Port 4	
Eigen Mode Expansion (EME) Solver	49.7	48.9	50.7	48.3	99.99
Finite difference Time Domain Method	49.3	48.5	50.4	48.8	99.99

APPENDIX C
SIMULATION METHODOLOGY

To simulate the complete device with S-bends, we use Eigen Mode Expansion (EME) solver to solve Maxwell's equations through a frequency domain method. In this algorithm, we decompose the electromagnetic field into the basis set of eigenmodes. To compute eigenmodes, we divide the geometry into separate cells and solve for the modes at the interface between adjacent cells. We then calculate the scattering matrices for each section by matching tangential electric (E) and magnetic (H) fields at the cell boundaries. After that, we propagate the solution of the scattering matrices bidirectionally and calculate the scattering matrix for the entire device. We use 15 nm mesh size in EME simulations. We also consider 50 cells on each side of the S-bend and 10 cells in the coupling region of our device.

We verify our simulation results with the Finite Difference Time Domain (FDTD) method. Table I represents the comparison between EME and FDTD simulation methods of our final device structure ($w = 475\ nm, h_e = 110\ nm, g = 40\ nm$, $L_c = 13.95\ \mu m$ and $L_s = 30\ \mu m$). We find a decent agreement between EME and FDTD methods. We use Lumerical FDTD and Mode solutions to perform these simulations.

APPENDIX D
DEVICE TOLERANCE

A. Change in Width (w) and Etch Depth (h_e)

We investigate the effect of width (w) and etch depth (h_e) on the fidelity of entangling two remote ions of our optimal device structure ($g = 40\ nm, L_s = 30\ \mu m$, and $L_c = 13.95\ \mu m$). Fig. 9 represents the fidelity with respect to the width and etch depth. We get the maximum fidelity at $w = 475\ nm$ and $h_e = 110\ nm$ which is the optimum case. If the device's width and etch depth are 10 nm away from their optimal values, we can still get >98% fidelity for entangling two remote ions. These findings suggest that our designed non-polarizing beam splitter is tolerant to fabrication imperfections which can result a change in width and etch depth.

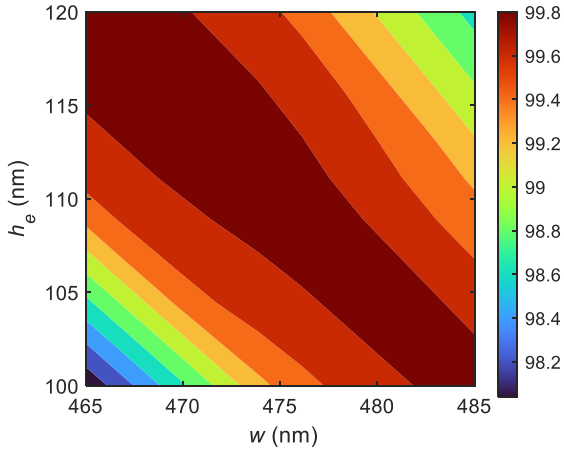

Fig. 9. Fidelity of entangling two ions with respect to width (w) and etch depth (h_e) of our optimal non-polarizing beam splitter ($g = 40\ nm$, $L_s = 30\ \mu m$, and $L_c = 13.95\ \mu m$).

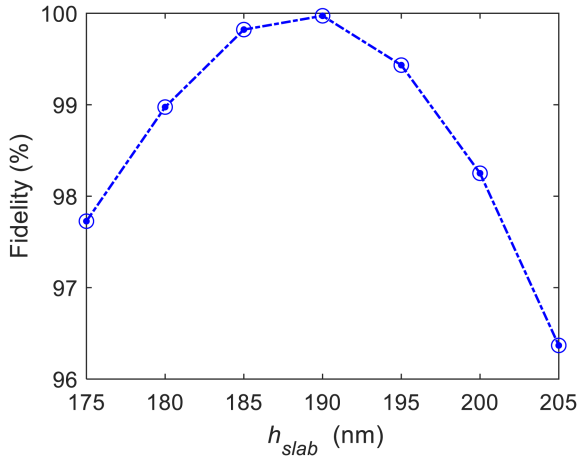

Fig. 10. Dependence of the fidelity as a function of slab thickness (h_{slab}) of the non-polarizing beam splitter ($w = 475\ nm$, $h_e = 110\ nm$, $g = 40\ nm$, $L_s = 30\ \mu m$ and $L_c = 13.95\ \mu m$). The total thickness of the thin film is $(h_e + h_{slab})\ nm$.

B. Change in Slab Thickness (h_{slab})

As the thickness of thin-film niobate may not be uniform across a wafer, we analyze the effect of slab thickness on the fidelity of the non-polarizing beam splitter (Fig. 10). For these simulations, we use the previous optimized parameters $w = 475\ nm$, $h_e = 110\ nm$, $g = 40\ nm$, $L_s = 30\ \mu m$ and $L_c = 13.95\ \mu m$. The total thickness of the thin-film lithium niobate can be found by adding the slab thickness (h_{slab}) with the etch depth (h_e). We observe >96.36% fidelity over 30 nm variation of the slab thickness.

C. Operating Wavelength

We examine the effect of operating wavelength on the device performance (Fig. 11) of the non-polarizing beam splitter

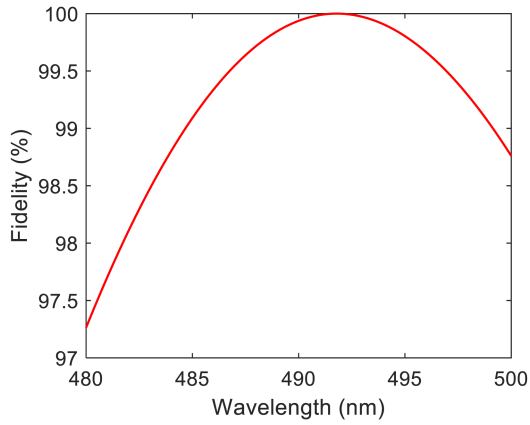

Fig. 11. Fidelity of entangling two ions with respect operating wavelength of our optimal non-polarizing beam splitter ($w = 475\ nm$, $h_e = 110\ nm$, $g = 40\ nm$, $L_s = 30\ \mu m$ and $L_c = 13.95\ \mu m$).

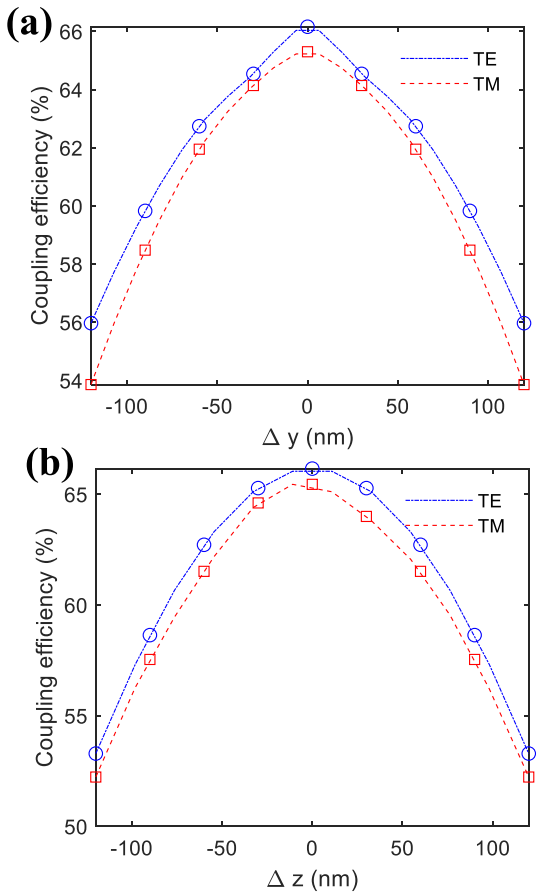

Fig. 12. Dependence of coupling efficiency to the waveguide as a function of deviation from optimal position (a) in Y-direction (Δy), (b) in Z-direction (Δz), when lensed fiber is placed at optimum z and y position, respectively.

($w = 475\ nm,\ h_e = 110\ nm,\ g = 40\ nm,\ L_s = 30\ \mu m$ and $L_c = 13.95\ \mu m$). Although our device is designed to work at the main transition wavelength (493.55 nm) of Barium ions, we can achieve fidelity of >97% over 480 nm to 500 nm wavelength range.

D. The Effect of Surface Roughness

Desiatov *et al.* reported the surface roughness of 7 Å in sidewalls and 6 dB/m loss in the visible wavelength range [17]. As our device is only ∼74 μm long, total loss due to the surface roughness can be negligible.

Appendix E
Dependence of Light Coupling Efficiency on Alignment Error

As alignment error between chip and fiber can induce polarization-dependent coupling efficiencies to the waveguide, we analyze the variation of coupling efficiency as a function of the alignment error (Fig. 12). We define Δy and Δz as the deviation from the optimal coupling position in the Y and Z- direction, respectively. We observe <2 % and <1 % polarization-dependent variation of coupling efficiency over 240 nm of Δy and Δz, respectively. That indicates that we can achieve polarization-independent light coupling to the waveguide with an alignment error. Apart from that, we can achieve >50% of coupling efficiency over ±120 nm of alignment error in the Y and Z-direction.

References

[1] P. Wang *et al.*, "Single ion qubit with estimated coherence time exceeding one hour," *Nature Commun.*, vol. 12, no. 1, pp. 1–8, 2021.
[2] C. Monroe and J. Kim, "Scaling the ion trap quantum processor," *Science*, vol. 339, no. 6124, pp. 1164–1169, 2013.
[3] T. Choi *et al.*, "Optimal quantum control of multimode couplings between trapped ion qubits for scalable entanglement," *Phys. Rev. Lett.*, vol. 112, May 2014, Art. no. 190502.
[4] C. Crocker, M. Lichtman, K. Sosnova, A. Carter, S. Scarano, and C. Monroe, "High purity single photons entangled with an atomic qubit," *Opt. Exp.*, vol. 27, no. 20, pp. 28143–28149, Sep. 2019.
[5] D. L. Moehring *et al.*, "Entanglement of single-atom quantum bits at a distance," *Nature*, vol. 449, no. 7158, pp. 68–71, 2007.
[6] M. Bock *et al.*, "High-fidelity entanglement between a trapped ion and a telecom photon via quantum frequency conversion," *Nature Commun.*, vol. 9, no. 1, pp. 1–7, 2018.
[7] C. J. Ballance, T. P. Harty, N. M. Linke, M. A. Sepiol, and D. M. Lucas, "High-fidelity quantum logic gates using trapped-ion hyperfine qubits," *Phys. Rev. Lett.*, vol. 117, Aug. 2016, Art. no. 060504.
[8] T. P. Harty *et al.*, "High-fidelity preparation, gates, memory, and readout of a trapped-ion quantum bit," *Phys. Rev. Lett.*, vol. 113, Nov. 2014, Art. no. 220501.
[9] R. J. Niffenegger *et al.*, "Integrated multi-wavelength control of an ion qubit," *Nature*, vol. 586, no. 7830, pp. 538–542, 2020.
[10] W. Bogaerts *et al.*, "Programmable photonic circuits," *Nature*, vol. 586, no. 7828, pp. 207–216, 2020.
[11] J. Wang, F. Sciarrino, A. Laing, and M. G. Thompson, "Integrated photonic quantum technologies," *Nature Photon.*, vol. 14, no. 5, pp. 273–284, 2020.
[12] P. Walther and A. Zeilinger, "Experimental realization of a photonic bell-state analyzer," *Phys. Rev. A*, vol. 72, Jul. 2005, Art. no. 010302.
[13] C. Monroe *et al.*, "Large-scale modular quantum-computer architecture with atomic memory and photonic interconnects," *Phys. Rev. A*, vol. 89, Feb. 2014, Art. no. 022317.
[14] J. L. O'brien, A. Furusawa, and J. Vučković, "Photonic quantum technologies," *Nature Photon.*, vol. 3, no. 12, pp. 687–695, 2009.
[15] N. C. Harris *et al.*, "Quantum transport simulations in a programmable nanophotonic processor," *Nature Photon.*, vol. 11, no. 7, pp. 447–452, 2017.
[16] J. Hannegan, U. Saha, J. D. Siverns, J. Cassell, E. Waks, and Q. Quraishi, "C-band single photons from a trapped ion via two-stage frequency conversion," *Appl. Phys. Lett.*, vol. 119, 2021, Art. no. 084001.
[17] B. Desiatov, A. Shams-Ansari, M. Zhang, C. Wang, and M. Lončar, "Ultra-low-loss integrated visible photonics using thin-film lithium niobate," *Optica*, vol. 6, no. 3, pp. 380–384, Mar. 2019.

[18] D. N. Nikogosyan, *Nonlinear Optical Crystals: A Complete Survey*. New York, NY, USA: Springer Science & Business Media, 2006.
[19] C. Wang *et al.*, "Integrated lithium niobate electro-optic modulators operating at cmos-compatible voltages," *Nature*, vol. 562, no. 7725, pp. 101–104, 2018.
[20] D. Zhu *et al.*, "Integrated photonics on thin-film lithium niobate," *Adv. Opt. Photon.*, vol. 13, no. 2, pp. 242–352, Jun. 2021. [Online]. Available: http://www.osapublishing.org/aop/abstract.cfm?URI=aop-13-2-242
[21] M. Zhang, C. Wang, R. Cheng, A. Shams-Ansari, and M. Lončar, "Monolithic ultra-high-q lithium niobate microring resonator," *Optica*, vol. 4, no. 12, pp. 1536–1537, Dec. 2017.
[22] V. Krutyanskiy, M. Meraner, J. Schupp, V. Krcmarsky, H. Hainzer, and B. Lanyon, "Light-matter entanglement over 50 km of optical fibre," *npj Quantum Inf.*, vol. 5, no. 1, pp. 1–5, 2019.
[23] M. Meraner *et al.*, "Indistinguishable photons from a trapped-ion quantum network node," *Phys. Rev. A*, vol. 102, Nov. 2020, Art. no. 052614. [Online]. Available: https://link.aps.org/doi/10.1103/PhysRevA.102.052614
[24] V. Krutyanskiy, M. Meraner, J. Schupp, and B. Lanyon, "Polarisation-preserving photon frequency conversion from a trapped-ion-compatible wavelength to the telecom C-band," *Appl. Phys. B*, vol. 123, no. 9, pp. 1–9, 2017.
[25] B. B. Blinov, D. L. Moehring, L.-M. Duan, and C. Monroe, "Observation of entanglement between a single trapped atom and a single photon," *Nature*, vol. 428, no. 6979, pp. 153–157, 2004.
[26] L. J. Stephenson *et al.*, "High-rate, high-fidelity entanglement of qubits across an elementary quantum network," *Phys. Rev. Lett.*, vol. 124, Mar. 2020, Art. no. 110501.
[27] I. Krasnokutska, J.-L. J. Tambasco, X. Li, and A. Peruzzo, "Ultra-low loss photonic circuits in lithium niobate on insulator," *Opt. Exp.*, vol. 26, no. 2, pp. 897–904, Jan. 2018.
[28] T. Fujisawa and M. Koshiba, "Polarization-independent optical directional coupler based on slot waveguides," *Opt. Lett.*, vol. 31, no. 1, pp. 56–58, Jan. 2006.
[29] L.-M. Chang, L. Liu, Y.-H. Gong, M.-Q. Tan, Y.-D. Yu, and Z.-Y. Li, "Polarization-independent directional coupler and polarization beam splitter based on asymmetric cross-slot waveguides," *Appl. Opt.*, vol. 57, no. 4, pp. 678–683, Feb. 2018.
[30] Q. Xu *et al.*, "Broadband polarization-independent directional coupler using asymmetric-waveguides," *IEEE Photon. J.*, vol. 11, no. 6, Dec. 2019, Art. no. 6603506.
[31] C.-W. Hsu, C.-F. Huang, W.-S. Tsai, and W.-S. Wang, "Lithium niobate polarization-independent modulator using integrated polarization splitters and mode converters," *J. Lightw. Technol.*, vol. 35, no. 9, pp. 1663–1669, 2017.
[32] S. Gao *et al.*, "Fast polarization-insensitive optical switch based on hybrid silicon and lithium niobate platform," *IEEE Photon. Technol. Lett.*, vol. 31, no. 22, pp. 1838–1841, Nov. 2019.
[33] L. Zhang, X. Fu, and L. Yang, "Polarization-independent, lithium-niobate-on-insulator directional coupler based on a combined coupling-sections design," *Appl. Opt.*, vol. 59, no. 28, pp. 8668–8673, Oct. 2020.
[34] A. Honardoost, K. Abdelsalam, and S. Fathpour, "Rejuvenating a versatile photonic material: Thin-film lithium niobate," *Laser Photon. Rev.*, vol. 14, no. 9, 2020, Art. no. 2000088.
[35] C. D. Bruzewicz, J. Chiaverini, R. McConnell, and J. M. Sage, "Trapped-ion quantum computing: Progress and challenges," *Appl. Phys. Rev.*, vol. 6, no. 2, 2019, Art. no. 021314.
[36] D. Hucul, J. E. Christensen, E. R. Hudson, and W. C. Campbell, "Spectroscopy of a synthetic trapped ion qubit," *Phys. Rev. Lett.*, vol. 119, Sep. 2017, Art. no. 100501. [Online]. Available: https://link.aps.org/doi/10.1103/PhysRevLett.119.100501
[37] E. Togan *et al.*, "Quantum entanglement between an optical photon and a solid-state spin qubit," *Nature*, vol. 466, no. 7307, pp. 730–734, 2010.
[38] S. Sun, H. Kim, Z. Luo, G. S. Solomon, and E. Waks, "A single-photon switch and transistor enabled by a solid-state quantum memory," *Science*, vol. 361, no. 6397, pp. 57–60, 2018.
[39] S. Dutta, E. A. Goldschmidt, S. Barik, U. Saha, and E. Waks, "Integrated photonic platform for rare-earth ions in thin film lithium niobate," *Nano Lett.*, vol. 20, no. 1, pp. 741–747, 2020.
[40] P. Maunz, D. Moehring, S. Olmschenk, K. Younge, D. Matsukevich, and C. Monroe, "Quantum interference of photon pairs from two remote trapped atomic ions," *Nat. Phys.*, vol. 3, no. 8, pp. 538–541, 2007.
[41] W.-P. Huang, "Coupled-mode theory for optical waveguides: An overview," *JOSA A*, vol. 11, no. 3, pp. 963–983, 1994.
[42] D. E. Zelmon, D. L. Small, and D. Jundt, "Infrared corrected Sellmeier coefficients for congruently grown lithium niobate and 5 mol.% magnesium oxide–doped lithium niobate," *J. Opt. Soc. Amer. B*, vol. 14, no. 12, pp. 3319–3322, Dec. 1997.
[43] D. Smith, H. Riccius, and R. Edwin, "Refractive indices of lithium niobate," *Opt. Commun.*, vol. 17, no. 3, pp. 332–335, 1976.
[44] I. H. Malitson, "Interspecimen comparison of the refractive index of fused silica," *J. Opt. Soc. Amer.*, vol. 55, no. 10, pp. 1205–1209, 1965.
[45] J. Carolan *et al.*, "Universal linear optics," *Science*, vol. 349, no. 6249, pp. 711–716, 2015.
[46] J. L. O'Brien, "Optical quantum computing," *Science*, vol. 318, no. 5856, pp. 1567–1570, 2007.
[47] S. Dutta, Y. Zhao, U. Saha, D. Farfurnik, E. A. Goldschmidt, and E. Waks, "An atomic frequency comb memory in rare-earth doped thin-film lithium niobate," 2021, *arXiv:2111.01942*.
[48] C. Hu *et al.*, "High-efficient coupler for thin-film lithium niobate waveguide devices," *Opt. Exp.*, vol. 29, no. 4, pp. 5397–5406, Feb. 2021.
[49] L. He, M. Zhang, A. Shams-Ansari, R. Zhu, C. Wang, and L. Marko, "Low-loss fiber-to-chip interface for lithium niobate photonic integrated circuits," *Opt. Lett.*, vol. 44, no. 9, pp. 2314–2317, May 2019. [Online]. Available: http://www.osapublishing.org/ol/abstract.cfm?URI=ol-44-9-2314
[50] X. Chen and H. K. Tsang, "Polarization-independent grating couplers for silicon-on-insulator nanophotonic waveguides," *Opt. Lett.*, vol. 36, no. 6, pp. 796–798, Mar. 2011. [Online]. Available: http://www.osapublishing.org/ol/abstract.cfm?URI=ol-36-6-796
[51] T. G. Tiecke *et al.*, "Efficient fiber-optical interface for nanophotonic devices," *Optica*, vol. 2, no. 2, pp. 70–75, Feb. 2015. [Online]. Available: http://www.osapublishing.org/optica/abstract.cfm?URI=optica-2-2-70